HAL
open science

Solidus melting of pyrolite and bridgmanite: Implication for the thermochemical state of the Earth's interior

Rémy Pierru, Laure Pison, Antoine Mathieu, Emmanuel Gardés, Gaston Garbarino, Mohamed Mezouar, Louis Hennet, Denis Andrault

To cite this version:

Rémy Pierru, Laure Pison, Antoine Mathieu, Emmanuel Gardés, Gaston Garbarino, et al.. Solidus melting of pyrolite and bridgmanite: Implication for the thermochemical state of the Earth's interior. Earth and Planetary Science Letters, 2022, 595, pp.117770. 10.1016/j.epsl.2022.117770 . hal-03759424

HAL Id: hal-03759424

https://hal.science/hal-03759424v1

Submitted on 21 Nov 2022

HAL is a multi-disciplinary open access archive for the deposit and dissemination of scientific research documents, whether they are published or not. The documents may come from teaching and research institutions in France or abroad, or from public or private research centers.

L'archive ouverte pluridisciplinaire **HAL**, est destinée au dépôt et à la diffusion de documents scientifiques de niveau recherche, publiés ou non, émanant des établissements d'enseignement et de recherche français ou étrangers, des laboratoires publics ou privés.

Solidus melting of pyrolite and bridgmanite: implication for the thermochemical state of the Earth's interior

Rémy PIERRU [1], Laure PISON [1], Antoine MATHIEU [1], Emmanuel GARDES [1,2], Gaston GARBARINO [3], Mohamed MEZOUAR [3], Louis HENNET [4] and Denis ANDRAULT [1,£]

[1] Université Clermont Auvergne, LMV, CNRS-OPGC-IRD, Clermont-Ferrand, France
[2] Normandie Université, ENSICAEN, CEA, CNRS, CIMAP, Caen, France
[3] European Synchrotron Radiation Facility, Grenoble, France
[4] Université d'Orléans, ICMN, CNRS, Orléans, France
[£] Corresponding author

Abstract

Melting properties of the deep mantle remain controversial due to experimental difficulties; e.g., reports of solidus temperatures of mantle-relevant compositions span over ~700K at 2000 km depth. This situation limits our understanding of the thermochemical state of the Earth's interior. Using the laser heated diamond anvil cell (LH-DAC), we performed new experimental determination of the solidus profile of ultra-dry pyrolite and the solidus of two compositions of (Mg,Fe)(Si,Al)O_3 bridgmanite (Bg). Melting was detected (i) from -the correlation between laser power and sample temperature, -changes of sample texture and -the level of visible light absorption, for all samples, (ii) using X-ray diffraction, for the $MgSiO_3$ composition and (iii) after scanning electron microscope observations, for selected Fe-bearing samples. Special care was given to using ultra-dry experimental chambers and to determination of sample temperature. In particular, we discuss the wavelength-dependent thermal emission of silicate samples, which lowers the solidus by 100 to 300K, compared to the grey-body assumption.

The solidus of $MgSiO_3$-Bg is in good agreement with previous reports using *ab initio* calculations and shock wave experiments. We observe a net decrease in the solid-liquid Clapeyron slope at 60(3) GPa and 4400(200) K, which can be related to rapid pressure-induced coordination change of Si in the melt. $(Mg_{0.955},Fe_{0.045})(Si_{0.993},Al_{0.007})O_3$ Bg melts 600-800 K lower than $MgSiO_3$-Bg. Its solidus evolves smoothly with pressure, suggesting progressive Si coordination change in the melt. In the pressure range investigated (24-135 GPa) Clapeyron slopes suggest rapid decrease of the volume of fusion, from 14 to 2% for $MgSiO_3$ and from 9 to 3% for (Fe,Al)-bearing Bg, assuming congruent melting. By comparing the solidii of various silicates, it appears that the higher the number of cations, the less pronounced is the curvature of the solidus. This observation suggests that the relatively ordered structure of simple liquid compositions with a limited number of distinct network-modifying cations frustrates the coexistence of tetrahedrally and octahedrally coordinated Si polyhedral.

The solidus of pyrolite presents a smooth evolution from 2200(100) K to 3950(200) K in the same pressure interval. This is very similar to our previous work on chondritic-type mantle. The new solidus is 200-300 K lower than that of KLB-1 peridotite, which can be related to more incompatible elements in pyrolite. It remains problematic that our solidus plots several 100 K higher than other recent measurements performed on pyrolite; we discuss the possibility of a higher water content in previous samples, compared to our experiments. Assuming a dry lowermost mantle, our results imply a core-mantle boundary temperature lower than 3950(200) K. Modeling the melting diagram at the core-mantle boundary suggests a pseudo-eutectic melt significantly depleted in SiO_2, compared to the composition of the mean mantle.

Highlights:

- Mantle solidus evolves from 2200(100) and 3950(200) K with depth in lower mantle
- Solidus of pyrolite suggests core-mantle boundary temperature lower than 3950(200)K
- The initially steep solidus of $MgSiO_3$ bridgmanite flattens at 60(3) GPa
- Silicate melts with more cations present smooth solidus evolution to CMB pressure

Introduction

Earth is very hot inside due to the major Moon forming impact that occurred 50-100 million years after its accretion. The impact melted its interior almost entirely (Nakajima and Stevenson, 2015). For this reason, mantle melting contributed largely to the internal dynamics of the Earth during its history. It is believed that partial melting is still occurring today in specific mantle regions such as in the ultra-low velocity zones (ULVZ) atop the core-mantle boundary (CMB; e.g. (Lay et al., 2004)) and the low-velocity layer between 350 and 410 km depth (LVL; e.g. (Tauzin et al., 2010)). Knowledge of the melting properties in the deep mantle is key to refine our knowledge of mantle history. In this work, we limit our analysis to the determination of the mantle solidus at lower mantle conditions.

There are not many reports on deep mantle melting, due to experimental and theoretical difficulties associated with (i) the very high pressure involved, up to 135 GPa at the core-mantle boundary (CMB), and (ii) the composition of the mantle with includes many elements. *Ab initio* calculations can be used to estimate the solidii of pure phases, such as $MgSiO_3$ bridgmanite (Bg) (Stixrude et al., 2009); However, it remains difficult to model the melting properties of more complex geological material. Similar limitation occurs for shock wave experiments, for which it is difficult to investigate a mixture of phases. Another limitation of shock waves is that melting is generally investigated along the Hugoniot; this limitation can be alleviated by sample pre-heating, pre-compression, ramp compression and thermodynamical modeling (Asimow, 2018).

Concerning static experiments, reproducing the P-T conditions typical of deep mantle melting requires today the use of the laser-heated diamond anvil cell (LH-DAC). LH-DAC has been used to determine melting properties for a long time, initially for simple compounds (e.g. (Zerr and Boehler, 1993)) and later for mantle relevant materials (Andrault et al., 2011; Fiquet et al., 2010; Nomura et al., 2014; Zerr et al., 1998). Still, there are major discrepancies between the different works. They can have several origins:

(i) Mantle composition: Previous works report the melting properties of either peridotitic, pyrolitic or chondritic-type mantle compositions. They differ in their (Mg,Fe,Ca)/Si ratio, which corresponds to variable fractions of the major minerals of the lower mantle: $(Mg,Fe)(Si,Al)O_3$ Bg, $CaSiO_3$ perovskite (very recently named davemaoite, Dvm) and (Mg,Fe)O ferropericlase (Fp). More Fp is expected when going from pyrolite, peridotite to harzburgite model compositions. Still, all these materials contain the same three phases and, therefore, their melting behavior should not be very different. The solidus temperature, in particular, could be very similar if eutectic-type melting prevails (Andrault et al., 2017; de Koker et al., 2013; Liebske and Frost, 2012). On the other hand, liquidus temperatures can be significantly different. The second aspect is the content of minor and incompatible elements. The more the material is depleted, from chondritic-type to pyrolite and peridotite, the purer the mineral phases (Bg, Fe and Dvm) must be (Corgne et al., 2005). This can affect the melting properties of each mineral and, in return, modify slightly the mantle solidus. The impact can be major when the mineral phases are saturated in a given incompatible element, which was reported unlikely for typical mantle compositions (Irifune, 1994). Altogether, we are facing small changes of composition. Slight changes of compositions between the materials relevant to the mean-mantle should have a limited impact on the solidus, as long as the concentration of incompatible elements remains below the limit of saturation of the mantle minerals (Irifune, 1994).

(ii) Melting criteria: several criteria have been used to detect the melting behavior: -change of optical properties, -correlation between laser power and sample temperature, with possible appearance of a temperature plateau and/or sudden temperature increase, -*in situ* monitoring of the phase content by X-ray diffraction, -density contrasts using nano-tomography, -microstructure of recovered samples using electron microscopy. Previous works generally use several of these criteria and report a good agreement between them in a same study. When using the LH-DAC, the detection of solidus is facilitated by the fact that the solid and liquid fractions absorb the laser radiation differently. The change of absorption coefficient of bulk sample upon melting induces a change of heating behavior that is clearly detectable (Geballe and Jeanloz, 2012). Consequently, it is unlikely that controversies about the solidus temperature arise from the melting criteria. The situation is much more complicated for the determination of the liquidus temperature, for which a robust criterion should inform on the complete disappearance (melting) of all minerals within the hot sample region, for a locally well-known chemical composition.

(iii) Experimental conditions: Beyond the definition of melting criteria, performing melting experiments using the LH-DAC remains difficult in many aspects. We emphasize two parameters that can have a major impact on determination of the solidus: water content and temperature measurements. Concerning the former, approaching "dry" conditions requires specific procedures. For example, annealing a powder in a vacuum oven is certainly insufficient to remove the water absorbed at the surface of sample grains. In addition, the

sample loading in air inevitably contaminates the sample with atmospheric water. Water can significantly lower the solidus, especially over the saturation limit of the mantle minerals. Concerning the latter; temperature measurements at very high temperature were shown to be more reliable when using reflective objectives, compared to refractive objectives (Giampaoli et al., 2018). In addition, refractive optics change their chromatic response when the optical path is slightly modified, which is common during LH-DAC experiments. The sample emissivity function should also be included in the temperature calculation.

In this work, we performed new measurements of the solidus temperature of several mantle materials, using *in house* optical, *in situ* X-ray diffraction and *post mortem* sample characterization techniques, in order to bring additional constraints on the melting behavior of the Earth's lower mantle.

Methods

Samples and DAC loading

We used a membrane-type DAC mounted with beveled diamonds and Re gaskets drilled using either spark erosion or laser ablation. Depending on the target pressure, we used beveled diamond anvils of 250/300, 150/300, 100/300 or 75/300 µm internal/external diameters, gasket thicknesses from 45 µm to 15 µm and hole diameters from 95 µm to 25 µm. One fresh piece of sample was used for each melting point determination. The nominal sample pressure was determined at 300 K from at least one of these methods: fluorescence of a ruby chip positioned in the pressure medium, Raman shift of the diamond anvil at the contact with the pressure medium (Suppl. Fig. 1), cell parameter of the KCl pressure medium determined using X-ray diffraction (Dewaele et al., 2012). Uncertainty in the determination of the nominal pressure at 300K is a couple of GPa. Then, some thermal pressure develops in the sample at high temperature, due to partially isochoric heating in the LH-DAC. We apply a pressure correction (ΔP_{corr}) of half the theoretical thermal pressure (ΔP_{Th}), $\Delta P_{corr}=0.5\Delta P_{Th}=0.5(\alpha K_T)_{Bg}(T_{Exp}-300)$ (Andrault et al., 2020), αK_T is the product of thermal expansion and isothermal bulk modulus of Bg (Fiquet et al., 2000), the most abundant phase in our samples, and T_{Exp} is the measured sample temperature. The final value of ΔP_{corr} is about 2.5 10^{-3} GPa per Kelvin above 300 K, with an uncertainty ± 5 % at the melting temperature.

As starting materials, we used a natural enstatite and two synthetic glasses; pyrolite and $MgSiO_3$. To probe the solidus of (Fe,Al)-bearing Bg, we selected a natural enstatite with low Fe and Al, namely $(Mg_{0.955},Fe_{0.045})(Si_{0.993},Al_{0.007})O_3$ (Table 1). The reason for this choice is an ambiguous solidus obtained in a previous study for a sample with high Fe and Al contents (Andrault et al., 2017), most probably because of incongruent melting and chemical migrations. The low Fe and Al contents in Bg are also relevant to melting conditions in the lower mantle, because of the relatively incompatible character of Fe and Al (Boujibar et al., 2016). On the other hand, the $MgSiO_3$ glass was synthesized in a classical furnace, while the glass of pyrolite (Table 1; (Ringwood, 1975)) was synthesized using the laser levitation technique. For the latter, the mixture of powders was carefully homogenized in an agate mortar and pre-compressed into a sphere. Levitation above a nozzle is performed by monitoring the flux of Ar with less than 0.05 ppm of oxygen, which yields a $Fe^{3+}/\Sigma Fe$ ratio of 7-8 % in the silicate glass. Using infrared spectroscopy, the water content in the glass is found between 18 and 22 ppm, based on the Beer-Lambert law and absorption coefficients given for basaltic and basanitic glasses. A fragment of the starting material was loaded in the gasket hole between two layers of the KCl pressure medium. KCl is a material of first-choice to study the melting properties of silicates in the LH-DAC: -a very high melting temperature at high pressures, -no chemical reactions with silicates when it is dry, -good thermal insulation between hot-samples and cold-diamonds. The sample thickness was chosen to be ~1/3 of the gasket thickness, in order to limit the axial thermal gradients. These gradients are invisible to optical observations and yet the most critical ones in the LH-DAC.

Table 1: Composition of starting material determined using the electron microprobe.

	Opx JF15-67 Wt%	Opx JF15-67 Mole%	Pyrolite Synth. Wt%	Pyrolite Synth. Mole%
SiO2	59.32	50.63	46.53	40.51
TiO2	0.00	0.00	0.01	0.01
Al2O3	0.33	0.17	4.55	2.34
Cr2O3	0.40	0.13	0.01	0.00
FeOt	3.10	2.21	8.57	6.24
MnO	0.06	0.00	0.02	0.01
MgO	36.47	46.40	37.55	48.74
CaO	0.35	0.32	2.11	1.97
Na2O	0.16	0.13	0.03	0.02
K2O	0.02	0.00	0.28	0.15
Total	100.22	99.99	99.66	100.00
Fe/(Mg+Fe)		0.045		0.113
Al/Fe		0.154		0.750
Al/(Al+Si)		0.007		0.104

We use special procedures to minimize the amount of water trapped in the pressure chamber: (i) all steps of the sample loading are performed inside a closed glove bag under a flux of dry air or N_2. All the

necessary material is dry and inserted in advance in the bag where a numerical water sensor is permanently operational. (ii) Coarse grains of KCl are kept in oven at 130-150 K all the time. (iii) The starting material and a KCl grain are crushed inside the glove bag. We do not crush the sample in fine powder that inevitably adsorb water. Instead, we load a shard of convenient size and shape in the gasket hole. Several criteria are typical of a dry system, like no adhesion between the loaded materials and a needle, except for a weak electrostatic bonding. Presence of humidity can also be detected optically at the surface of the diamond culet. Then, when we would measure a melting temperature lower compared to previous measurements, we reload the cell with new sample and loading tools, to check the melting temperature in another experiment.

Optical set-up, laser heating and temperature measurements

We used two optical set-ups (i) for melting $MgSiO_3$ at ID27 and (ii) for all other experiments in LMV. Both systems follow the basic principles established several years ago (Schultz et al., 2005): in particular, they are both equipped with reflective optics. It was shown that they are superior to refractive optics for determination of very high temperatures in the LH-DAC (Giampaoli et al., 2018). The new laser heating system of LMV (Suppl. Fig. 2) is optimized for simultaneous temperature measurements on both sample sides (using the TRax software (Holtgrewe et al., 2019)). On ID27, temperature was measured on both sample sides prior to performing angle-dispersive X-ray diffraction with monitoring of temperature on one sample side only. The $MgSiO_3$ sample was first heated using a CO_2-laser (10µm radiation) until crystallization of small grains of Bg made the sample slightly opaque to visible light. Then, two fiber lasers (IPG fiber photonic lasers YLR-100-AC producing 1.03µm radiation) could heat the sample up to the melting point. Similarly, fiber lasers were used to study the melting behavior of (Fe,Al)-bearing Bg and pyrolite. The two lasers arrive with an angle of incidence of about 15° with respect to the cell axis and are focused on the sample using silica lenses with a focal length of 75 mm, or 50 mm when the pressure exceeds ~80 GPa. The laser paths are remotely controlled using piezoelectric actuators.

Temperatures up to 5200 K were measured from the sample thermal emission in the visible range (600 to 1000 nm; Suppl. Figs. 3-5). We dedicated a special care to cross-calibrate the optical response of ID27 and LMV optical systems. For this, we used (i) a platinum heating wire calibrated on the melting points of wollastonite (1817 K) and diopside (1664 K), (ii) a newly acquired commercial lamp calibrated on a formal black body and (iii) an additional tungsten lamp calibrated at LMV and measured at ID27, and vice versa. In addition, we reworked the general assumptions made on the sample emissivity function ($\varepsilon(\lambda)$), which most commonly are (i) a grey-body sample (constant $\varepsilon(\lambda)$) or (ii) same $\varepsilon(\lambda)$ for the sample and the W-lamp. We found that the second one is more in agreement with the data available for $\varepsilon(\lambda)$ of silicates (see (Andrault et al., 2022)). For a sample showing a wavelength-dependent (WD) emissivity, using the black body (BB) assumption yields temperature (T_{BB}) overestimated by ~65, ~151, ~280 and ~464 K for a true sample temperature (T_{WD}) of 2000, 3000, 4000 and 5000 K, respectively; the 2nd-order polyhedral relation between T_{BB} and T_{WD} is: $T_{BB}-T_{WD}=2.585\ 10^{-5}*T_{WD}^2-4.814\ 10^{-2}*T_{WD}+60.46$. A further argument in favor of wavelength-dependent $\varepsilon(\lambda)$ for silicates is the solidii of SiO_2 (Andrault et al., 2022) and $MgSiO_3$ (see Result section below) falling in very good agreement with shock wave experiments (Akins and Ahrens, 2002) and ab initio calculations (e.g. (Usui and Tsuchiya, 2010)). Following this observation, we will propose a temperature correction to the previous reports of the solidii of peridotite (Fiquet et al., 2010) and chondritic-type mantle (Andrault et al., 2011).

Another major source of uncertainty comes from temperature gradients: Both optical systems used in this study analyze the thermal emission signal coming from a sample region of 2-3 microns diameter at the center of the laser spot, which minimizes the effect of radial temperature gradient. On the contrary, axial temperature gradients produce superimposition of thermal radiation spectra coming from sample regions at different temperatures, when probing an optically transparent sample. Still, the distortion could remain minor because the hottest region of the sample (i.e. where melting occurs first) provides the strongest contribution to thermal emission.

We note that the sample microstructure becomes heterogeneous after melting, due to melt migration. It affects the laser-absorption as well as the thermal emissivity function, potentially; It can yield distortion of the thermal emission spectrum. For this reason, we always use a fresh piece of sample for each determination of the melting temperature.

Finally, we noticed a higher temperature uncertainty when using the lasers at high power (when approaching 100 watts). Reasons for this can be (i) stronger axial temperature gradients in the DAC, yielding less stable temperature at the center of the sample, (ii) convection of air between the diamond cell and the schwarzchild objectives, inducing optical fluctuation, (iii) difficulties to detect the temperature vs laser-

power plateau. For this reason, we favor loadings with thick layers of insulating KCl on both sides of a thin sample. Taking all possible precautions, the uncertainty of a given temperature measurement at the highest temperatures is ~50 K (Suppl. Fig. 3).

Melting criteria

To investigate melting of pure $MgSiO_3$-Bg, we monitored the change of structural properties using X-ray diffraction at the ID27 beamline, using the same procedure as in our recent work on SiO_2 (Andrault et al., 2020). With increasing temperature, the diffraction rings progressively evolve from coarse and rounded for the compressed glass, continuous and very fine for nano-crystalline Bg, spotty after severe grain growth of Bg grains and, finally, a few diffraction spots, which change positions very fast with time when the sample gets molten. X-ray diffuse scattering of the melt also appears at the melting point (Andrault et al., 2020; Fiquet et al., 2010); However, we do not use amplitude of X-ray diffuse scattering and full disappearance of all diffraction peaks as major criteria. The reason is the axial temperature gradient between the two diamonds, which inevitably induce crystallization close to cold diamonds, while the melting temperature is already reached at the center of the sample.

For Fe-bearing samples, crystallization was detected by changes in the absorption properties. Next, we performed incremental steps of 0.2 to 0.4 watts during careful monitoring of the temperature, with a special care to detect any anomaly in the sample behavior. An entire experiment generally takes ~30 minutes with a time interval of 30 to 60 seconds between two temperatures. At a sample pressure of e.g. 138 GPa, three distinct sample behaviors can be distinguished (Fig. 1a, see also Suppl. Figs. 4 and 5): (i) a regular increase of temperature for laser power between 12 and 32 watts. (ii) a plateau with no significant increase of temperature for laser power between 32 to 52 watts. On the plateau, temperature fluctuations are less than 5%. This plateau is interpreted as a progressive increase of the melt fraction in the sample with laser power, with a melt absorbing less the laser radiation than the solid part. This can happen for (Fe,Al)-Bg that contains both Fe^{2+} and Fe^{3+} in large amounts, which implies good absorption of the 1 µm laser radiation. Less Bg implies a higher laser power for maintaining a similar sample temperature. This behavior was well established based on the combination of several other melting criteria and modeling of the sample behavior (Andrault et al., 2014; Geballe and Jeanloz, 2012; Thomson et al., 2014). (iii) a larger fluctuation of the sample temperature with further increase of the laser power, before a jump to temperatures 1000 to 2000 K higher than the temperature plateau. This arises when the laser power becomes sufficient to heat the melt above the solidus. Another possible explanation is a low thermal conductivity of the melt, which would induce a higher sample temperature in the sample center (Shen and Lazor, 1995). Altogether, the solidus temperature and its uncertainty, between 50 to 150 K, are determined after averaging the highest temperatures measured on the plateau.

After laser shutdown, the sample microstructure provides another criterion for occurrence of melting (Fig. 1b). In particular, the presence of a dark blob at the center of the laser spot is a good indicator of melt migration. The blob is often surrounded by a lighter shell of material, likely Bg depleted in Fe (Nabiei et al., 2021). We further characterized the microstructure of selected samples using high-resolution scanning electron microscope (SEM) at CIMAP, following previous works of the same kind (Fiquet et al., 2010; Nomura et al., 2011; Tateno et al., 2014). For this, we prepared thin sections using the focused Ga-ion beam FIB. Cuts were performed perpendicularly to the sample surface across the laser-heated area, which yields an observable sample surface along the paths of the infrared lasers between the two diamonds. Melting induces solid-melt segregation, with a higher Fe-concentration in the melt easily detectable in the SEM (Fig. 1c, (Nabiei et al., 2021)). We note that the microstructure of the molten regions can be complex due to fast recrystallization upon quenching.

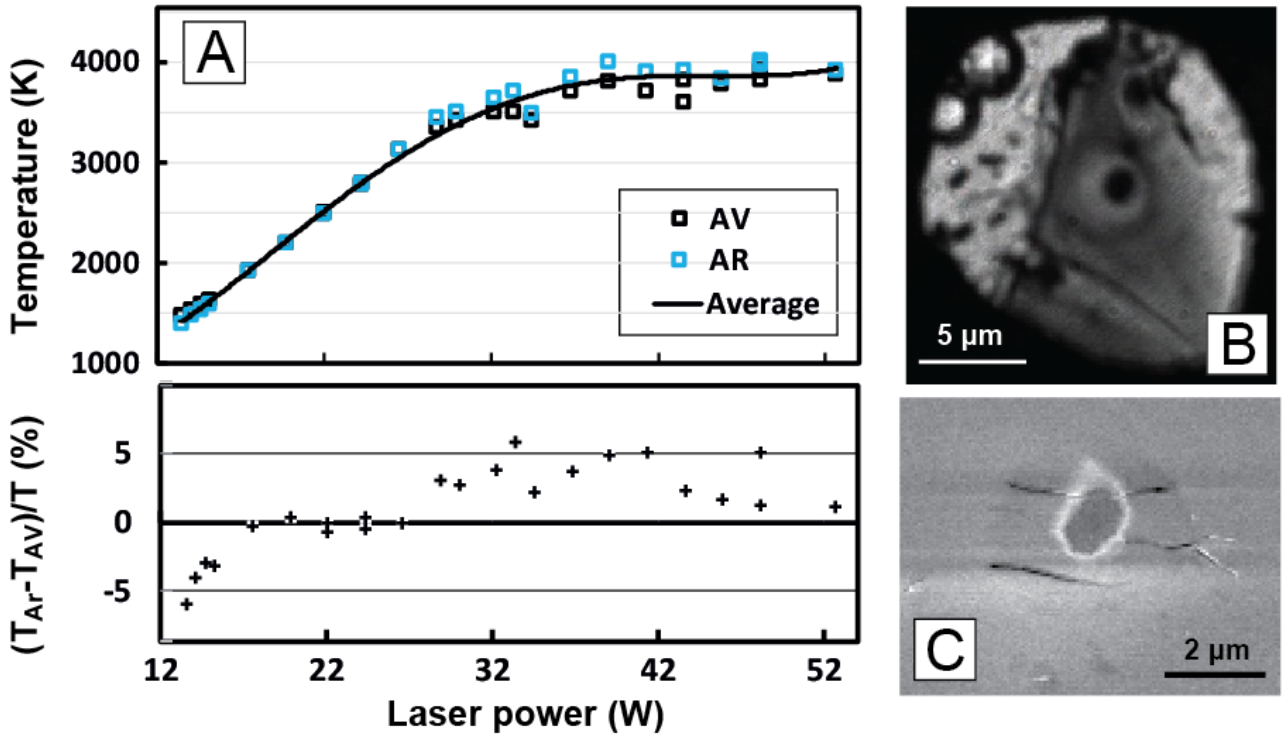

Figure 1: Melting criteria for LMV experiments: (a) Temperature as a function of increasing laser power for a sample of pyrolite loaded at 138 GPa, yielding a solidus melting temperature of 3950(200) K. "Av" and "Ar" temperatures are measured on each side of the sample. On bottom left, we report the temperature difference between the two sides of the sample (b) Optical microphotograph showing a black spot at the center of the sample after melting at 94 GPa. (c) SEM microphotograph (secondary electrons) of the melted region at 65 GPa. There is central blob of melt enriched in Fe (darker zone; as in (Nabiei, 2017)), surrounded by a first shell of Fe-depleted bridgmanite (lighter zone) and the un-molten pyrolite sample further from the sample. Other examples of the experimental determination of solidii are reported in Suppl. Figs. 4 and 5.

Results

Solidus of $MgSiO_3$ bridgmanite

The solidus of $MgSiO_3$ was determined from 10 different measurements performed at pressures between 35 GPa and 3400K, and 140 GPa and 5200 K (Fig. 2, Table 2). The data plot within the range of melting temperature proposed in previous studies. Up to ~60 GPa, the slope of our solidus is comparable with previous LH-DAC measurements on Al-free Bg (Shen and Lazor, 1995; Zerr and Boehler, 1993), even though our melting temperature plots 200-300 K lower. This corresponds to a steep Clapeyron slope of ~42 K/GPa between ~25 and 60 GPa. At high mantle pressures, our $MgSiO_3$-Bg solidus is in good agreement with previous *ab initio* calculations (de Koker and Stixrude, 2009) and shock wave experiments (Mosenfelder et al., 2009). Between 60 and 140 GPa, the Clapeyron slope becomes ~10 K/GPa. Due to the change of slope, we modeled the solidus using two different modified Simon and Glatzel equations [$T=T_0(P/a+1)^{1/c}$] (Simon and Glatzel, 1929): T_0= 274 K, a= 0.2644 GPa and c= 1.9575 between 35 and 60 GPa, and T_0= 403 K, a= 0.00028 GPa and c= 5.1377 between 60 and 140 GPa (Table 3). We note that while the (T_0, a, b) parameters constrain the melting temperature at a given pressure, the slope and the curvature of the melting curve, each parameter has no formal significance when taken independently of the other two, especially for melting curves restricted to high pressure regions.

This change of behavior around 60 GPa denotes a marked change in the thermodynamic parameters, most probably a decrease of the volume of fusion (ΔV_m), or a decrease in entropy of fusion, with increasing pressure. Such effect could be due to higher compression rate of the melt, compared to Bg. A major ingredient of melt compaction is the change of Si coordination number from 4 to 6. Our $MgSiO_3$ solidus suggests a relatively abrupt Si coordination change in the melt at ~60 GPa. Using the Clapeyron relation ($dT/dP=\Delta V_m/\Delta S_m$) and an entropy change upon melting (ΔS_m) of 63.7 J/molK (Stixrude et al., 2009), we estimate the volume of fusion for $MgSiO_3$. Based on the Simon and Glatzel equations, we obtain $\Delta V_m/V_{Bg}$ (with V_{Bg} the molar volume of Bg) decreasing from 15% to 2% with increasing pressure from 25 to 135 GPa, respectively (Fig. 3). The abruptness of the ΔV_m change at ~60 GPa is overestimated due to the use of different equations above and below the transition pressure.

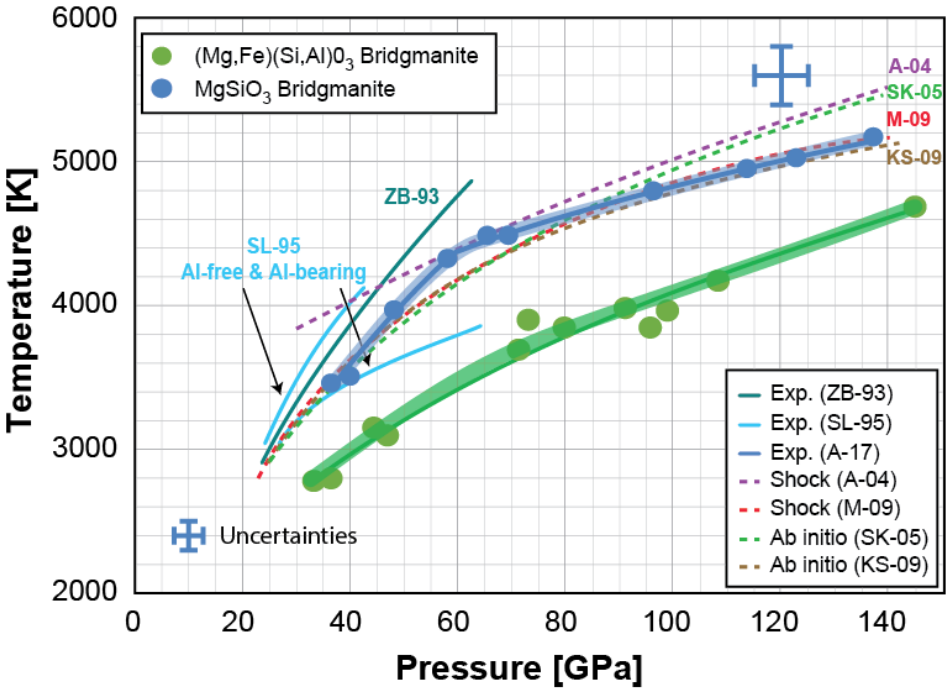

Figure 2: Solidus of bridgmanite: We report our work on $MgSiO_3$ (blue dots) and $(Mg_{0.955},Fe_{0.045})(Si_{0.993},Al_{0.007})O_3$ (green dots) bridgmanite together with previous studies: LH-DAC on $(Mg_{0.88}Fe_{0.12}SiO_3)$ (ZB-93, (Zerr and Boehler, 1993)), $MgSiO_3$ and $Mg_3Al_2Si_3O_{12}$ (SL-95; (Shen and Lazor, 1995)), shock waves on $MgSiO_3$ (AK-04; (Akins et al., 2004), M-09; (Mosenfelder et al., 2009)) and *ab initio* calculations for $MgSiO_3$ (KS; (de Koker and Stixrude, 2009), SK-05; (Stixrude and Karki, 2005)).

Solidus of $(Mg_{0.955},Fe_{0.045})(Si_{0.993},Al_{0.007})O_3$ bridgmanite

Twelve different measurements have been performed to determine the solidus of our (Fe,Al)-bearing Bg compound. We note that this (Fe,Al)-bearing compound may not melt congruently at the solidus, however, our experimental method cannot resolve the finite melting interval between the solidus and the liquidus. The solidus is found between 500 and 1000 K lower than that of $MgSiO_3$, even though this enstatite sample presents relatively low Fe and Al contents, compared to mantle composition. Still, the several minor elements present in this natural phase (Table 1) may also play a role in reducing the melting temperature. The solidus appears more linear in the pressure range investigated, compared to $MgSiO_3$, which points out a more progressive melt compaction. We acknowledge that our data set presents some scattering between 70 and 100 GPa, which may be related to chemical heterogeneities in the starting material. For this reason, we reproduced the measurements several times. Nevertheless, the maximum temperature difference remains within a reasonable range of uncertainties of 200-300 K. The entire solidus can be satisfactorily fitted using a single Simon and Glatzel equation with T_0= 241 K, a= 0.03145 GPa and c= 2.8501 (Table 3). Its Clapeyron slope evolves from ~28 to ~12 K/GPa in the pressure range investigated. Finally, we calculate ΔV_m based on the same value of ΔS_m as for $MgSiO_3$. As expected from the difference in the solidii, ΔV_m decreases more progressively with increasing the pressure, compared to $MgSiO_3$ (Fig. 3).

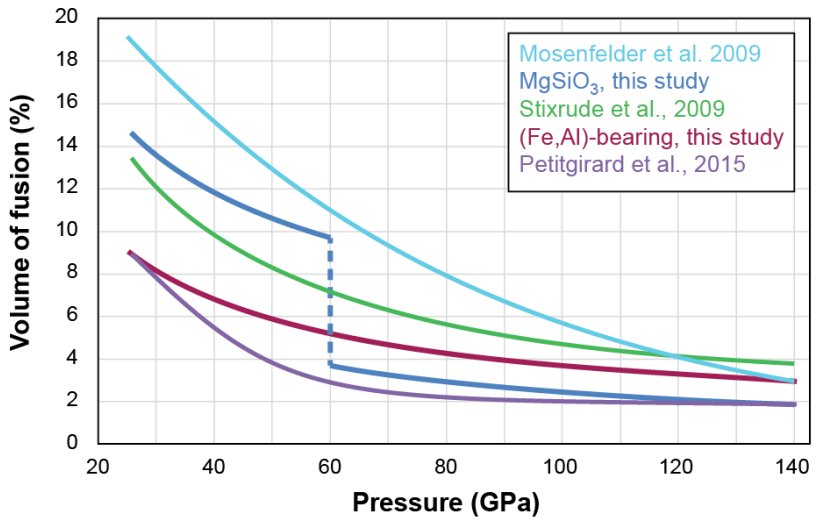

Figure 3: Volume of fusion ($\Delta V_m/V_{Bg}$) for bridgmanite. We report our data for $MgSiO_3$ and $(Mg_{0.955},Fe_{0.045})(Si_{0.993},Al_{0.007})O_3$ bridgmanite phases and $MgSiO_3$ $\Delta V_m/V_{Bg}$ obtained based on shock-wave experiments (Mosenfelder et al., 2009), ab initio calculations (Stixrude et al., 2009) and glass density measurements (Petitgirard et al., 2015). For $MgSiO_3$ data, our calculation overestimates the sharpness of the transition at ~60 GPa.

Solidus of dry pyrolite

We performed 39 determination of the melting for our pyrolite glass (Table 2). In the lower mantle, pyrolite yields a mineral assemblage made of Bg, Dvm and Fp. As a result, progressive sample melting is expected between the solidus and liquidus temperatures. In this study, we dedicated our experimental efforts to the determination of the solidus profile (Fig 4). It exhibits a smooth evolution from 2200(100) K to 3950(200) K for pressures between 24 GPa (the 660 km depth discontinuity) to 140 GPa (close to CMB), respectively. The solidus presents a significant curvature, which corresponds to a Clapeyron slope evolving from 28 to 13 K/GPa in the pressure range investigated, which is very similar to the values obtained for our (Fe,Al)-Bg compound. Still, the solidus of pyrolite plots 500-600 K lower. In addition to 3 phases, instead of one for (Fe,Al)-bearing Bg, pyrolite contains a significantly larger amount of incompatible elements, which can also contribute to lowering the solidus.

In the low pressure range, our solidus plots in very good agreement with our recent determination of the solidus at pressures up to 27 GPa, using the multi-anvil apparatus (Pierru et al., 2022). We note that higher melting temperatures were proposed for the melting of mantle-relevant materials in the upper mantle and transition zone (e.g. (Litasov and Ohtani, 2002; Tronnes and Frost, 2002)). The discrepancy may arise from several factors, including a rather high melt fraction reported in previous work. This matter is discussed at length elsewhere (Andrault et al., 2018; Pierru et al., 2022). To provide a convenient model for the pyrolite solidus at all mantle pressures, we coupled the two data sets on the same pyrolitic sample and fitted two Simon and Glatzel equations (Fig. 4). We obtain T_0= 1609 K, a= 61.1176 GPa and c= 1.1288 for the pressure range between 5 and 24 GPa and T_0= 235 K, a= 0.0300 GPa and c= 3.0067 between 24 and 138 GPa (Table 3).

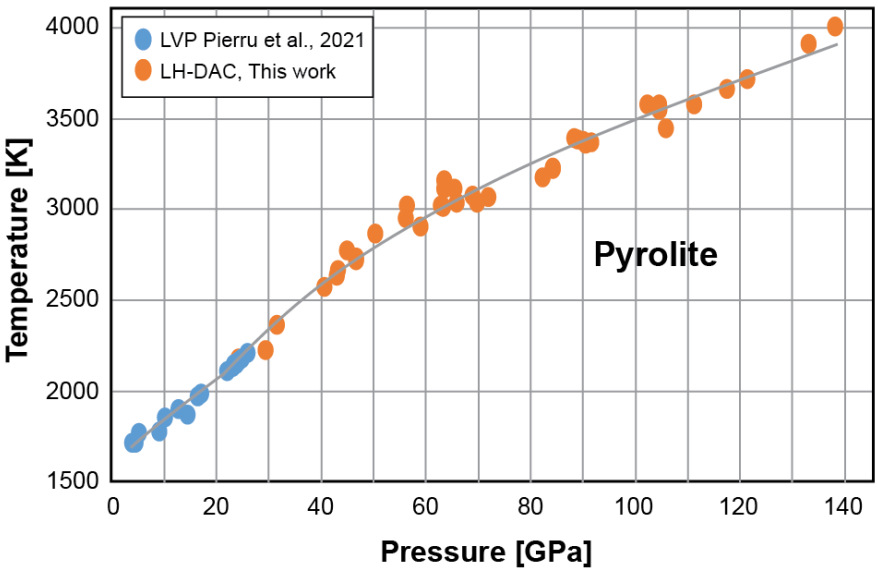

Figure 4: **Solidus of pyrolite:** Data sets from multi-anvil press ((Pierru et al., 2022), blue dots) and diamond anvil cell from this work (orange dots) are combined to determine the solidus of pyrolite at all mantle-relevant pressures.

Table 2: **Experimental data**: Summary of all experimental measurements of solidii reported in this work

MgSiO3		(Fe,Al)-bearing Bg		Pyrolite			
P(GPa)	T(K)	P(GPa)	T(K)	P(GPa)	T(K)	(continued)	
58.1	4321	33.2	2780	24.1	2184	69.0	3080
65.5	4479	36.5	2800	29.4	2230	69.8	3039
96.2	4790	33.2	2780	31.5	2364	71.9	3072
113.6	4942	36.5	2800	40.6	2579	82.2	3175
122.8	5018	45.1	3152	43.0	2638	84.3	3225
137.2	5167	47.0	3100	43.1	2670	84.3	3230
40.0	3504	71.5	3700	45.0	2775	88.3	3385
69.5	4479	73.4	3900	46.7	2721	88.9	3378
36.4	3462	79.9	3850	46.7	2738	90.1	3373
48.2	3959	91.2	3986	50.4	2867	90.4	3357
		95.9	3850	56.1	2955	91.7	3366
		99.2	3966	56.3	3021	102.2	3579
		108.7	4171	59.0	2906	104.6	3530
		145.0	4691	62.8	3023	104.7	3565
				63.2	3016	105.9	3450
				63.4	3118	111.2	3575
				63.6	3163	117.4	3664
				65.4	3116	121.5	3715
				65.9	3041	133.0	3900
						138.3	4000

Table 3: **Melting equations**: Summary of the parameters refined for Simon&Glatzel melting equations through data points of $MgSiO_3$ and our (Fe,Al)-bearing Bg, and pyrolite.

Simon et Glatzel equations			
Compound	MgSiO3	(Fe,Al)-Bg	Pyrolite
P-range (GPa)	35-60	32-145	5-24.
T0 (K)	274	241	1609
a (GPa)	0.2644	0.03145	61.118
c	1.9575	2.8501	1.1288
P-range (GPa)	60-140		24-138
T0 (K)	403		235
a (GPa)	0.00028		0.0300
c	5.1377		3.0067

Discussion

Mantle solidus: Comparison between different studies

We compare our pyrolite solidus with other recent determinations of the solidus for various mantle relevant compositions (Fig. 5). We make the following observations: (i) Our solidus plots 300-400 K lower than that reported for peridotite (F-10; (Fiquet et al., 2010)). (ii) It is very compatible with many studies between 20 and 50 GPa; however the different studies diverge at higher mantle pressures to become (iii) 100-150 K lower than that reported for chondritic-type mantle (A-11; (Andrault et al., 2011)) and (iv) 300-500 K higher than other reports for pyrolite by (N-14; (Nomura et al., 2014)) and (K-20; (Kim et al., 2020)) at the CMB conditions. At this point, we note that F-10, A-11 and our new study were performed in very similar conditions, in particular with same type of synthetic starting material and similar optical systems mounted with reflective objectives. A major difference, however, is how the sample emissivity $\varepsilon(\lambda)$ was considered to calculate temperatures from thermal emission. F-10 and A-11 assume a grey-body function (i.e. $\varepsilon(\lambda)$=constant), while this method could induce artifacts (Deng et al., 2017). Unfortunately, $\varepsilon(\lambda)$ is not known for silicates at the high P-T investigated in this study. So far, the most appropriated assumption could be same $\varepsilon(\lambda)$ as the W-lamp (see (Andrault et al., 2022)). We calculate a temperature correction, of a couple 100 K, that would account for wavelength-dependent thermal emission of peridotite and chondritic-type mantle in previous studies (light orange and purple bands in Fig. 5). For A-11, we also include in the calculation the solidus data points reported for the same sample based on multi-anvil press work (Andrault et al., 2018). Interestingly, the corrected chondritic-type solidus falls in perfect agreement with our pyrolite solidus. This result is coherent with the small difference between these two compositions, which have a similar fertility (amount of minor incompatible elements) and for which the main differences are the Bg, Dvm and Fp phase fractions. Concerning F-10 data, the corrected values plot 200-300 K above ours, which could be due to a more depleted peridotite composition. The three data sets (F-10, A-11 and our pyrolite data) converge to a solidus temperature of 3950(200) K at the 135 GPa of the CMB.

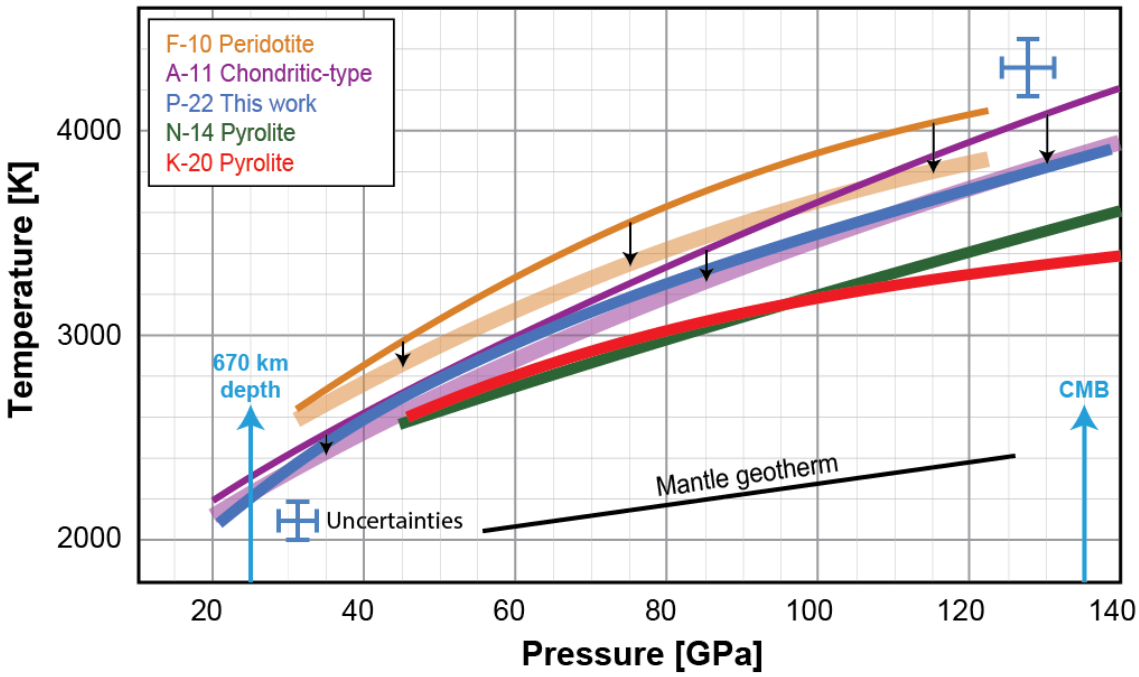

Figure 5: Solidus temperatures of various mantle materials. We plot the new pyrolite solidus (P-22) together with previous reports (F-10, (Fiquet et al., 2010); A-11, (Andrault et al., 2011); N-14, (Nomura et al., 2014); K-20, (Kim et al., 2020)). For F-10 and A-11, we report both the original solidii (thin orange and purple lines) and the corrected solidii (light but thicker lines indicated by black arrows) for which temperatures have been recalculated taking take into account the wavelength-dependent thermal emission (see text).

The N-14 and K-20 data sets that plot significantly lower than ours, for which the most likely explanation is the presence of some water in these experiments. Noticeably, the K-20 data set plots at lower

temperatures than N-14, for which the reported water content in the sample is 400 ppm. In K-20 work, vacuum oven was used to dry powders before loading and then to dry the entire DAC after loading. In our previous experience on melting of chondritic-type mantle (Andrault et al., 2011), we did not succeeded to reproduce the solidus using starting materials made of powders, and always found much lower temperatures. Our explanation is that annealing temperatures much higher than e.g. 150°C (i.e. oven) are needed to remove the water adsorbed at the surface of the grains. Fine powders can adsorb a significant amount of water in a few minutes. For this reason, we use chips of glass for the loading in the DAC and all loadings are performed in a glove bag flushed with inert atmosphere.

Comparison of the curvatures of solidii

We plot together the solidii of various silicate phases. To strengthen the comparison, we selected the works performed using the same methodology (Fig. 6); in addition to compositions discussed above, we include SiO_2 (see (Andrault et al., 2020) and its "comment" taking into account its wavelength-dependent behavior (Andrault et al., 2022)) and mid-ocean ridge basalt (MORB; (Andrault et al., 2014), also corrected here for its $\varepsilon(\lambda)$). As logically expected, the larger the amount of cations entering in the sample composition [N_{Cat}], from 1 to 6 between pure SiO_2 and our pyrolite sample, the lower is the solidus. Another interesting observation is the curvature of the melting slope, which (i) is significantly less pronounced and (ii) appears at higher pressure, with increasing N_{Cat}. A sharp change of the Clapeyron slope is found around 40 GPa for SiO_2, it is also clear at 60 GPa for $MgSiO_3$, one could argue for a deviation in the 60-80 GPa range for $(Mg_{0.955},Fe_{0.045})(Si_{0.993},Al_{0.007})O_3$ Bg, and the solidi present a progressive change between ~40 and ~100 GPa for mantle-relevant peridotitic, chondritic-type, or pyrolitic compositions. Since this curvature denotes a change of the volume of fusion with increasing pressure, the observed trend is consistent with a more abrupt change in the cation coordination number when N_{Cat} is smaller. The major structural change at mantle depth being the Si coordination change from 4 to 6, it suggests that the coexistence in the melt of the two structural entities, SiO_4 and SiO_6, is facilitated for a larger number of cations. Interestingly, the MORB solidus is significantly more curved than the mean-mantle relevant compositions. This effect could arise from a higher SiO_2 content in this material.

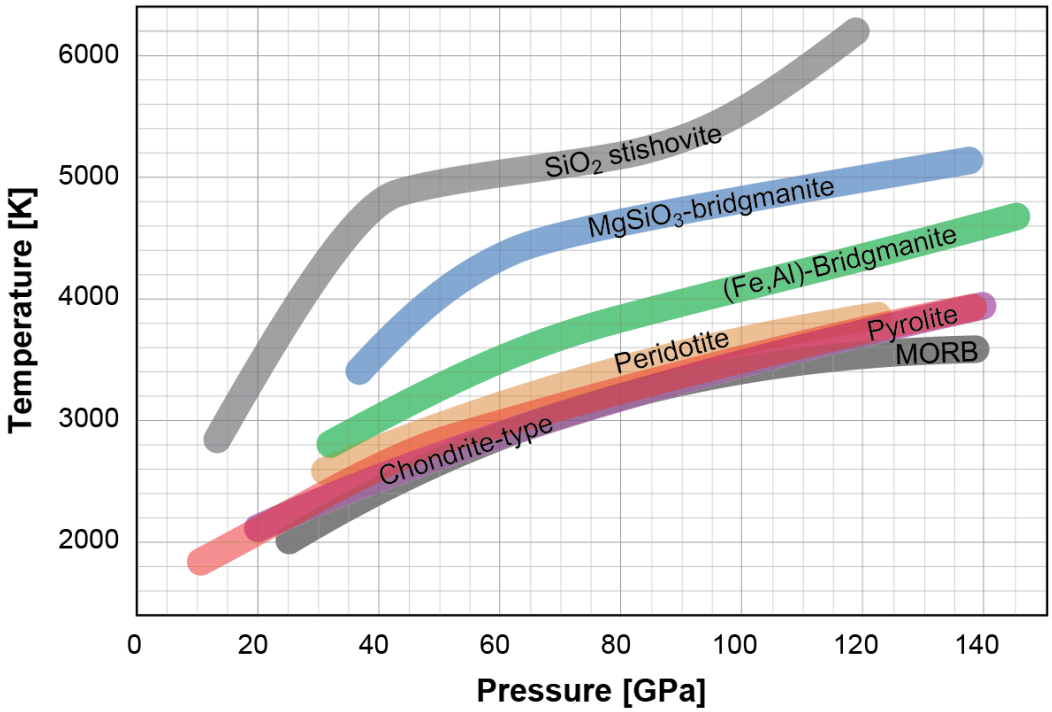

Figure 6: Solidii of various silicates. To improve the strength of the comparison, we only report the solidii of silicate phases determined using the same experimental techniques, in particular (i) reflective objectives that offer a best temperature measurement at high temperature (Giampaoli et al., 2018) and (ii) dry glasses loaded using a glove bag flowed by inert atmosphere. SiO_2 (Andrault et al., 2020; Andrault et al., 2022), peridotite (Fiquet et al., 2000), chondritic-type mantle (Andrault et al., 2011), MORB (Andrault et al., 2014) and $MgSiO_3$, $(Mg_{0.955},Fe_{0.045})(Si_{0.993},Al_{0.007})O_3$, and pyrolite (this work).

Building the melting diagram at mantle depth: example of the core-mantle boundary

Several approaches have been developed to discuss the thermodynamics of mantle melting in the lower mantle. One of them consists in refining the thermodynamical properties of silicate melts with end-member compositions, such as $MgSiO_3$, MgO, SiO_2, etc., using either first-principles molecular dynamics simulations or shock-wave experiments (Asimow, 2018; de Koker et al., 2013; Mosenfelder et al., 2009; Stixrude et al., 2009; Stixrude and Karki, 2005). Then, melting properties of mantle-relevant compositions can be modeled based on well-defined mixing properties between the end-members. In this work, we provide directly the solidii, which unfortunately does not help to constrain the basic thermodynamic parameters, but which can help constraining the melting diagrams.

If we leave to further works the goal to solve the controversy about the solidus of pyrolite, there is an overall good coherence on the solidii of the different silicate compositions (Fig. 6). If we focus on the CMB, data sets (F-10, A-11 and this work) converge to a solidus mantle temperature of 3950(200) K (Fig. 5). In these conditions, the melt composition is not well constrained and it anyway depends on the degree of partial melting. Nevertheless, previous studies performed at less extreme pressures suggest a pseudo-eutectic melt composition close to peridotite, based on multi-anvil press (Ito et al., 2004) and LH-DAC experiments (e.g. (Tateno et al., 2014)). Based on this, we draw a pseudo-binary phase diagram between $MgSiO_3$-Bg and a mixture of the other oxides (Fig. 7; see details of the strategy in (Andrault et al., 2017)). We model a linear solidus profile from the melting temperature of $MgSiO_3$-Bg and our (Fe,Al)-bearing Bg. Similarly, a linear liquidus profile is drawn from melting point of $MgSiO_3$-Bg to the liquidus temperature of the chondritic-type mantle (Andrault et al., 2011). The linear extrapolation of the liquidus to a pseudo-eutectic temperature of 3950 K yields an estimated composition of the pseudo-eutectic melt. Here, we do not consider the liquidus temperature of ~5400 K proposed for peridotite at the CMB (Fiquet et al., 2010), because such experimental temperature corresponds more likely to the melting temperature of pure Bg.

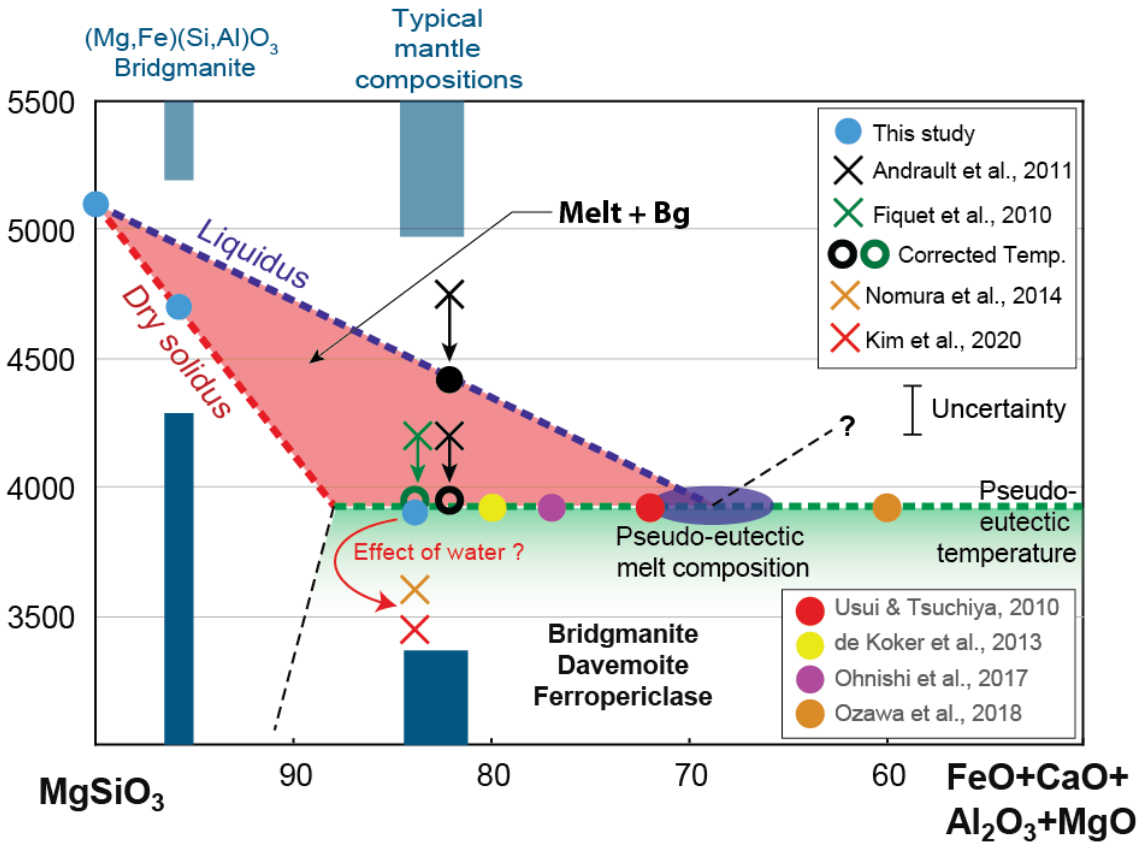

Figure 7: Melting diagram of silicate mantle at the CMB pressure of 135 GPa: A pseudo binary diagram is presented in which one pole is $MgSiO_3$ bridgmanite and a second one regroups all other elements (FeO, CaO, Al_2O_3 and MgO). The left blue vertical line corresponds to the composition of bridgmanite investigated in this study. The second vertical line corresponds to typical mantle compositions. We compare our estimate of the melt composition at the pseudo-eutectic temperature (purple ellipse) with previous reports in the MgO-$MgSiO_3$ system (de Koker et al., 2013; Ohnishi et al., 2017; Ozawa et al., 2018; Usui and Tsuchiya, 2010).

The melting diagram (Fig. 7) yields important information: -the higher the Bg content, the closer the solidus temperature is to that of the $MgSiO_3$-Bg end-member. -The Bg grains in equilibrium with mantle melts should be significantly enriched in Fe and Al with decreasing temperature below the liquidus. -The pseudo-eutectic melt composition at the CMB should be significantly depleted in SiO_2 (i.e. enriched in FeO, CaO, MgO and/or Al_2O_3), compared to classical models of mean mantle composition. Our estimated value plots within the interval of values reported for the simplified MgO-$MgSiO_3$ composition at the CMB (de Koker et al., 2013; Ohnishi et al., 2017; Ozawa et al., 2018; Usui and Tsuchiya, 2010) -Finally, the difference between solidus and liquidus reaches a maximum of ~700 K for a mantle composition with ~90% of $MgSiO_3$ and it decreases progressively with increasing the Fp and Dvm contents up to the pseudo-eutectic composition (where solidus and liquidus temperatures are equal).

Thermal state of the core-mantle boundary

Extrapolation of the mantle geotherm along an adiabatic gradient to the 135 GPa yields a value of ~2630 K(60) at the CMB, based on the elastic parameters of the mantle constituent minerals (Katsura et al., 2010). This does not take into account a possible super-adiabatic temperature gradient in the lower mantle. By performing global inversion of seismic radial profiles based on compressional and shear properties of the minerals, the lowermost mantle temperature was refined between 2800 and 3400 K (Matas et al., 2007). Such type of modeling is poorly sensitive to the rapid change of temperature occurring in the thermal boundary layer extending a few 100 km above the CMB. It was proposed that the Bg to post-Bg transition, which is sharp for $MgSiO_3$ composition, provides a constraint for the temperature in this region (Hernlund, 2010). Supposing that the loop-shaped low-velocity regions of the lowermost mantle correspond to a double crossing between the mantle temperature profile and the Clapeyron slope of this transition, the CMB temperature is estimated at ~3700 K (Tateno et al., 2009). Unfortunately, the Bg to post-Bg transition is progressive and occurs at too high pressures for a relevant (Fe,Al)-bearing mantle compositions (Andrault et al., 2010; Catalli et al., 2009), which shed doubts on this method. From core properties, the CMB temperature is estimated to ~4050 K, based on the melting point of a relevant Fe-alloy at the inner-core boundary (Anzellini et al., 2013).

A CMB temperature of 4050 K would be similar or higher than the mantle solidus, which we refine at 3950(200) K for 135 GPa in this study (Fig. 5). It would induce global mantle melting at the contact of the core, which is incompatible with seismic observations of ULVZ (e.g. (Yu and Garnero, 2018)). Instead, the CMB temperature should be lower than ~3950 K. Uncertainties remain regarding the fertility of the mantle located above the CMB, which could range from undepleted primitive to recycled peridotite compositions. The more the material is depleted, the higher its solidus and the higher could be the CMB temperature. The material that lies on the CMB could also be of a different nature, which we discuss below. Anyhow, it is very possible that the mantle geotherm reaches ~3950 K at the CMB, given the strong temperature increase when approaching the CMB. Then, a local enrichment in incompatible and/or volatile elements could depress the mantle solidus by several 100 K and induce melting in specific regions, producing the ultra-low velocity zones (Yu and Garnero, 2018). The nature of the chemical heterogeneities remains uncertain. Many of the incompatible elements, such as Na and K, may have a moderate effect on the solidus temperature, as they can be incorporated into the structure of Dvm (Corgne et al., 2005; Irifune, 1994). In contrast, H_2O could depress the mantle solidus significantly, possibly down to 3400-3500 K if we assume that water explains the difference between our study and the previous experimental works (Kim et al., 2020; Nomura et al., 2014). Finally, the melting of basalt was reported at a temperature of 3600 K (corrected from (Andrault et al., 2014) for wavelength-dependent $\varepsilon(\lambda)$), which is slightly lower than the melting point of the mantle. Altogether, this brackets the CMB temperature between 3600 and 3950 K, or between 3400-3500 and 3950 K, if melting of e.g. pyrolitic in ULVZ is triggered by a high concentration of incompatible elements, or water, respectively.

Acknowledgments: We thank P.D. Asimow, K.K.M. Lee and an anonymous reviewer for their thoughtful comments. This research was financed by the French Government Laboratory of Excellence initiative n°ANR-10-LABX-0006, the French ANR project EquipEx GENESIS (ANR-11-EQPX-0020), the Région Auvergne and the European Regional Development Fund. This is Laboratory of Excellence ClerVolc contribution N°XX.

References cited:

Akins, J.A., Ahrens, T.J., 2002. Dynamic compression of SiO_2: A new interpretation. Geophys. Res. Lett. 29, 1394.

Akins, J.A., Luo, S.N., Asimow, P.D., Ahrens, T.J., 2004. Shock-induced melting of $MgSiO_3$ perovskite and implications for melts in Earth's lowermost mantle. Geophys. Res. Lett. 31, L14612.

Andrault, D., Bolfan-Casanova, N., Bouhifd, M.A., Boujibar, A., Garbarino, G., Manthilake, G., Mezouar, M., Monteux, J., Parisiades, P., Pesce, G., 2017. Toward a coherent model for the melting behavior of the deep Earth's mantle. Phys. Earth Planet. Inter. 265, 67-81.

Andrault, D., Bolfan-Casanova, N., Lo Nigro, G., Bouhifd, M.A., Garbarino, G., Mezouar, M., 2011. Melting curve of the deep mantle applied to properties of early magma ocean and actual core-mantle boundary. Earth Planet. Sci. Lett. 304, 251-259.

Andrault, D., Morard, G., Garbarino, G., Mezouar, M., Bouhifd, M.A., Kawamoto, T., 2020. Melting behavior of SiO_2 up to 120 GPa. Phys. Chem. Mineral. 47, 10.

Andrault, D., Munoz, M., Bolfan-Casanova, N., Guignot, N., Perrillat, J.P., Aquilanti, G., Pascarelli, S., 2010. Experimental evidence for perovskite and post-perovskite coexistence throughout the whole D'' region. Earth Planet. Sci. Lett. 293, 90-96.

Andrault, D., Pesce, G., Bouhifd, M.A., Bolfan-Casanova, N., Henot, J.M., Mezouar, M., 2014. Melting of subducted basalt at the core-mantle boundary. Science 344, 892-895.

Andrault, D., Pesce, G., Manthilake, G., Monteux, J., Bolfan-Casanova, N., Chantel, J., Novella, D., Guignot, N., King, A., Itie, J.-P., Hennet, L., 2018. Deep and persistent melt layer in the Archaean mantle. Nat. Geosci. 11, 139-+.

Andrault, D., Pison, L., Morard, G., Garbarino, G., Mezouar, M., Bouhifd, M.A., Kawamoto, T., 2022. Comment on: Melting behavior of SiO2 up to 120 GPa (Andrault et al. 2020). Phys. Chem. Mineral. 49, 3.

Anzellini, S., Dewaele, A., Mezouar, M., Loubeyre, P., Morard, G., 2013. Melting of Iron at Earth's Inner Core Boundary Based on Fast X-ray Diffraction. Science 340, 464-466.

Asimow, P.D., 2018. Chapter 15 - Melts Under Extreme Conditions From Shock Experiments, in: Kono, Y., Sanloup, C. (Eds.), Magmas Under Pressure. Elsevier, pp. 387-418.

Boujibar, A., Bolfan-Casanova, N., Andrault, D., Bouhifd, M.A., Trcera, N., 2016. Incorporation of Fe^{2+} and Fe^{3+} in bridgmanite during magma ocean crystallization. Am. Miner. 101, 1560-1570.

Catalli, K., Shim, S.H., Prakapenka, V.B., 2009. Thickness and Clapeyron slope of the post-perovskite boundary. Nature 462, 782-785.

Corgne, A., Liebske, C., Wood, B.J., Rubie, D.C., Frost, D.J., 2005. Silicate perovskite-melt partitioning of trace elements and geochemical signature of a deep perovskitic reservoir. Geochim. Cosmochim. Acta 69, 485-496.

de Koker, N., Karki, B.B., Stixrude, L., 2013. Thermodynamics of the MgO-SiO_2 liquid system in Earth's lowermost mantle from first principles. Earth Planet. Sci. Lett. 361, 58-63.

de Koker, N., Stixrude, L., 2009. Self-consistent thermodynamic description of silicate liquids, with application to shock melting of MgO periclase and $MgSiO_3$ perovskite. Geophys. J. Int. 178, 162-179.

Deng, J., Du, Z., Benedetti, L.R., Lee, K.K.M., 2017. The influence of wavelength-dependent absorption and temperature gradients on temperature determination in laser-heated diamond-anvil cells. Journal of Applied Physics 121, 025901.

Dewaele, A., Belonoshko, A.B., Garbarino, G., Occelli, F., Bouvier, P., Hanfland, M., Mezouar, M., 2012. High-pressure high-temperature equation of state of KCl and KBr. Phys. Rev. B 85.

Fiquet, G., Auzende, A.L., Siebert, J., Corgne, A., Bureau, H., Ozawa, H., Garbarino, G., 2010. Melting of Peridotite to 140 Gigapascals. Science 329, 1516-1518.

Fiquet, G., Dewaele, A., Andrault, D., Kunz, M., Le Bihan, T., 2000. Thermoelastic properties and crystal structure of $MgSiO_3$ perovskite at lower mantle pressure and temperature conditions. Geophys. Res. Lett. 27, 21-24.

Geballe, Z.M., Jeanloz, R., 2012. Origin of temperature plateaus in laser-heated diamond anvil cell experiments. Journal of Applied Physics 111, 123518.

Giampaoli, R., Kantor, I., Mezouar, M., Boccato, S., Rosa, A.D., Torchio, R., Garbarino, G., Mathon, O., Pascarelli, S., 2018. Measurement of temperature in the laser heated diamond anvil cell: comparison between reflective and refractive optics. High Pressure Res 38, 250-269.

Hernlund, J.W., 2010. On the interaction of the geotherm with a post-perovskite phase transition in the deep mantle. Phys. Earth Planet. Inter. 180, 222-234.

Holtgrewe, N., Greenberg, E., Prescher, C., Prakapenka, V.B., Goncharov, A.F., 2019. Advanced integrated optical spectroscopy system for diamond anvil cell studies at GSECARS. High Pressure Res 39, 457-470.

Irifune, T., 1994. Absence of an aluminous phase in the upper part of the Earth's lower mantle. Nature 370, 131-133.

Ito, E., Kubo, A., Katsura, T., Walter, M.J., 2004. Melting experiments of mantle materials under lower mantle conditions with implications for magma ocean differentiation. Phys. Earth Planet. Inter. 143-144, 397-406.

Katsura, T., Yoneda, A., Yamazaki, D., Yoshino, T., Ito, E., 2010. Adiabatic temperature profile in the mantle. Phys. Earth Planet. Inter. 183, 212-218.

Kim, T., Ko, B., Greenberg, E., Prakapenka, V., Shim, S.H., Lee, Y., 2020. Low Melting Temperature of Anhydrous Mantle Materials at the Core-Mantle Boundary. Geophys. Res. Lett. 47.

Lay, T., Garnero, E.J., Williams, Q., 2004. Partial melting in a thermo-chemical boundary layer at the base of the mantle. Phys. Earth Planet. Inter. 146, 441-467.

Liebske, C., Frost, D.J., 2012. Melting phase relations in the MgO-$MgSiO_3$ system between 16 and 26 GPa: Implications for melting in Earth's deep interior. Earth Planet. Sci. Lett. 345, 159-170.

Litasov, K., Ohtani, E., 2002. Phase relations and melt compositions in CMAS–pyrolite–H_2O system up to 25 GPa. Phys. Earth Planet. Inter. 134, 105-127.

Matas, J., Bass, J.D., Ricard, Y., Mattern, E., Bukowinsky, M.S., 2007. On the bulk composition of the lower mantle: predictions and limitations from generalized inversion of radial seismic profiles. Geophys. J. Int. 170, 764-780.

Mosenfelder, J.L., Asimow, P.D., Frost, D.J., Rubie, D.C., Ahrens, T.J., 2009. The $MgSiO_3$ system at high pressure: Thermodynamic properties of perovskite, postperovskite, and melt from global inversion of shock and static compression data. J. Geophys. Res. 114, B01203.

Nabiei, F., 2017. From 2D to 3D Characterization of Materials Subjected to Extreme Pressure and Temperature Conditions. 230.

Nabiei, F., Badro, J., Boukaré, C.-É., Hébert, C., Cantoni, M., Borensztajn, S., Wehr, N., Gillet, P., 2021. Investigating Magma Ocean Solidification on Earth Through Laser-Heated Diamond Anvil Cell Experiments. Geophys. Res. Lett. 48, e2021GL092446.

Nakajima, M., Stevenson, D.J., 2015. Melting and mixing states of the Earth's mantle after the Moon-forming impact. Earth Planet. Sci. Lett. 427, 286-295.

Nomura, R., Hirose, K., Uesugi, K., Ohishi, Y., Tsuchiyama, A., Miyake, A., Ueno, Y., 2014. Low Core-Mantle Boundary Temperature Inferred from the Solidus of Pyrolite. Science 343, 522-525.

Nomura, R., Ozawa, H., Tateno, S., Hirose, K., Hernlund, J.W., Muto, S., Ishii, H., Hiraoka, N., 2011. Spin crossover and iron-rich silicate melt in the Earth's deep mantle. Nature 473, 199-202.

Ohnishi, S., Kuwayama, Y., Inoue, T., 2017. Melting relations in the MgO-MgSiO3 system up to 70 GPa. Phys. Chem. Mineral. 44, 445-453.

Ozawa, K., Anzai, M., Hirose, K., Sinmyo, R., Tateno, S., 2018. Experimental Determination of Eutectic Liquid Compositions in the MgO-SiO2 System to the Lowermost Mantle Pressures. Geophys. Res. Lett. 45, 9552-9558.

Petitgirard, S., Malfait, W.J., Sinmyo, R., Kupenko, I., Hennet, L., Harries, D., Dane, T., Burghammer, M., Rubie, D.C., 2015. Fate of MgSiO3 melts at core–mantle boundary conditions. Proceedings of the National Academy of Sciences 112, 14186-14190.

Pierru, R., Andrault, D., Manthilake, G., Monteux, J., Devidal, J.L., Henry, L., Guignot, N., King, A., 2022. Mantle origin of ancient large igneous provinces. Submitted.

Ringwood, A.E., 1975. Pyrolite and the Chondritic Earth Model, in: GrawHill, M. (Ed.), International series in the Earth's and Planetary Sciences, pp. 189-194.

Schultz, E., Mezouar, M., Crichton, W., Bauchau, S., Blattmann, S., Andrault, D., Fiquet, G., Boehler, R., Rambert, N., Sitaud, B., Loubeyre, P., 2005. Double-sided laser heating system for in situ high pressure-high temperature monochromatic x-ray diffraction at the ESRF. High Pressure Res 25, 71-83.

Shen, G., Lazor, P., 1995. Measurement of melting temperatures of some minerals under lower mantle conditions. J. Geophys. Res. 100, 17699-17713.
Simon, F., Glatzel, G., 1929. Fusion-pressure curve. Zeitschrift für anorganische und allgemeine Chemie 178, 309-316.
Stixrude, L., de Koker, N., Sun, N., Mookherjee, M., Karki, B.B., 2009. Thermodynamics of silicate liquids in the deep Earth. Earth Planet. Sci. Lett. 278, 226-232.
Stixrude, L., Karki, B.B., 2005. Structure and freezing of $MgSiO_3$ liquid in the Earth's lower mantle. Science 310, 297-299.
Tateno, S., Hirose, K., Ohishi, Y., 2014. Melting experiments on peridotite to lowermost mantle conditions. J. Geophys. Res. 119, 4684-4694.
Tateno, S., Hirose, K., Sata, N., Ohishi, Y., 2009. Determination of post-perovskite phase transition boundary up to 4400 K and implications for thermal structure in D " layer. Earth Planet. Sci. Lett. 277, 130-136.
Tauzin, B., Debayle, E., Wittlinger, G., 2010. Seismic evidence for a global low-velocity layer within the Earth's upper mantle. Nat. Geosci. 3, 718-721.
Thomson, A.R., Walter, M.J., Lord, O.T., Kohn, S.C., 2014. Experimental determination of melting in the systems enstatite-magnesite and magnesite-calcite from 15 to 80 GPa. Am. Miner. 99, 1544-1554.
Tronnes, R.G., Frost, D.J., 2002. Peridotite melting and mineral–melt partitioning of major and minor elements at 22–24.5 GPa. Earth Planet. Sci. Lett. 197, 117-131.
Usui, Y., Tsuchiya, T., 2010. Ab Initio Two-Phase Molecular Dynamics on the Melting Curve of SiO_2. J. Earth Sci. 21, 801-810.
Yu, S.L., Garnero, E.J., 2018. Ultralow Velocity Zone Locations: A Global Assessment. Geochem., Geophys., Geosyst. 19, 396-414.
Zerr, A., Boehler, R., 1993. Melting of $(Mg,Fe)SiO_3$-perovskite to 625 kbar: Indication of a high melting temperature in the lower mantle. Science 262, 553–555.
Zerr, A., Diegeler, A., Boehler, R., 1998. Solidus of earth's mantle. Science 281, 243-246.

Solidus melting of pyrolite and bridgmanite: implication for the thermochemical state of the Earth's interior

Rémy PIERRU [1], Laure PISON [1], Antoine MATHIEU [1], Emmanuel GARDES [1,2], Gaston GARBARINO [3], Mohamed MEZOUAR [3], Louis HENNET [4] and Denis ANDRAULT [1,£]

Supplementary material caption: The supplementary material contains several figures:

- Suppl. Fig. 1: Pressure measurement using Raman spectroscopy
- Suppl. Fig. 2: LH-DAC experimental set-up developed at the LMV
- Suppl. Fig. 3: Investigation of the uncertainty of temperature measurement
- Suppl. Fig. 4: Series of thermal emission spectra recorded up to the solidus temperature
- Suppl. Fig. 5: Typical laser power vs temperature plateaus

Supplementary Figures

Suppl. Fig. 1: **Pressure measurement using Raman spectroscopy.** Pressure is calculated from the shift of the inflection point (blue lines) of Raman spectrum recorded at room (red) and high (black) pressure. Raman spectra are recorded on the surface of the diamond culet as close as possible from the sample. In this example, the inflection point shifts from 1310.8 +/-0.5 cm^{-1} and 1524.5 +/-2.0 cm^{-1} yielding a nominal pressure (at 300K) of 108.7 +/- 2.5 GPa.

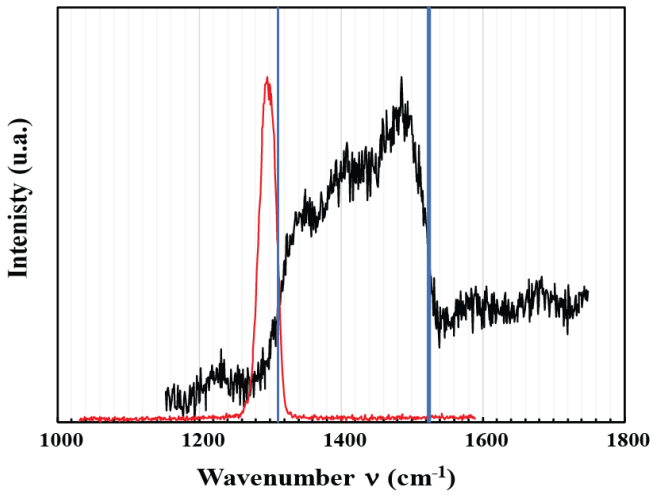

Suppl. Fig. 2: LH-DAC experimental set-up developed at the LMV. Main components are the water-cooled diamond anvil cell, two fiber lasers focused on the compressed sample with an angle of ~15 degrees, two reflective Schwarzschild objectives, a camera to visualize the laser spots on both sample sides and a spectrometer to determine the sample pressure and temperature on both sides simultaneously.

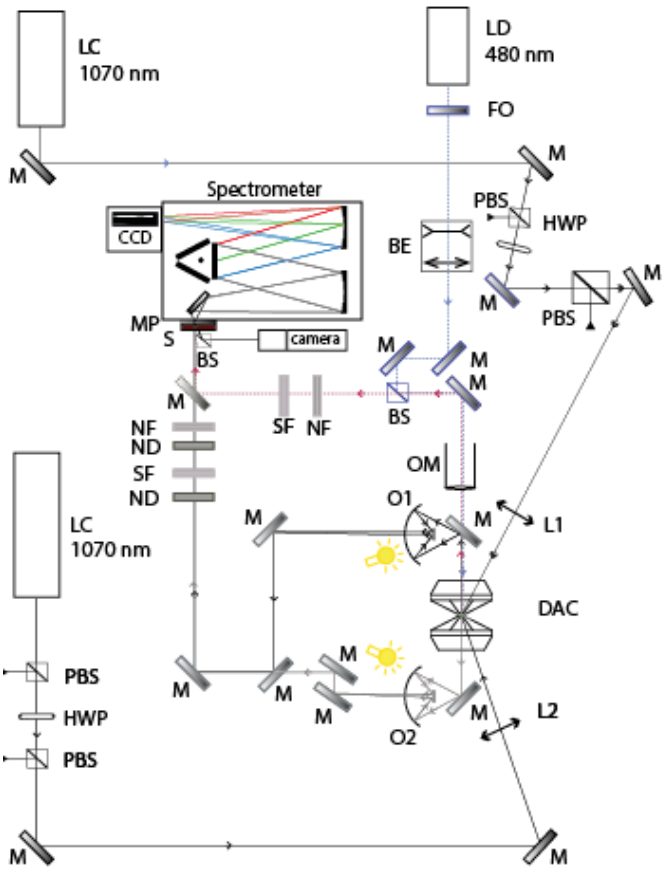

LC : Yb Fiber Laser, 100W
LD : Diode Laser, 200mW
DAC : Diamond Anvil Cell
O1- 2 : Reflective objective
OM : HR Refractive objective
BS : Beam Splitter 50/50
PBS : Polarized Beam Splitter
HWP : Half-Wave Plate
BE : Beam Expander
M : Mirrors

Spectrometer: double grating
CCD: camera
MP : Mirror with Pinholes
S : External Shutter
L : Convex Lens: f=50 or 75mm
FO : Clean-up Filter
SF : Short range pass Filter
NF : Notch Filter
ND : Neutral Density Filter
Camera : with Zoom

Suppl. Fig. 3: Investigation of the uncertainty of temperature measurement. A same thermal emission spectrum recorded at the solidus of pyrolite at ~138 GPa is fitted using 4 different ranges of wavelengths: from 640, 660, 680 or 700 nm to ~990 nm. The 4 adjustments yield temperatures between 4017 and 4080 K. The best fit is obtained when using the narrowest range of wavelengths; however, the fit quality may be misleading. When using a wider range of wavelengths, the quality of the fit is degraded due to a lower signal intensity at wavelengths shorter than ~700 nm. This effect could arise from a stronger interaction between light and electrons at high light energies, inducing a relatively low sample emissivity (i.e. high sample absorption). Still, this type of effects are not known well and could also affect other regions of the recorded thermal emission spectra. As a compromise, it arises that a sample temperature of 4040 +/- 25 K is compatible with the fits performed over a wide range of wavelengths.

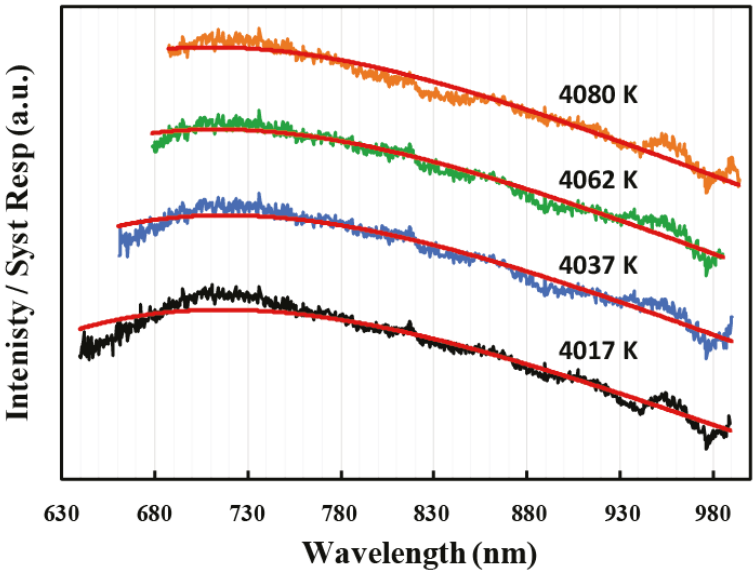

Suppl. Fig. 4: **Series of thermal emission spectra recorded up to the solidus temperature: (a)** Bridgmanite at 45 GPa **(b)** Pyrolite at 138 GPa.

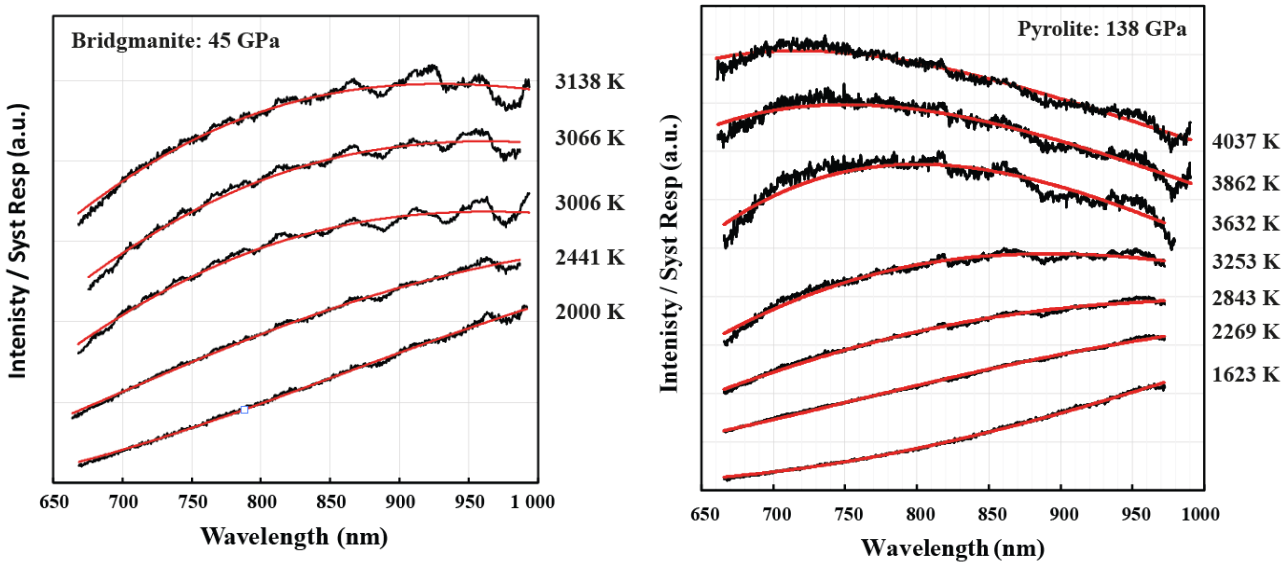
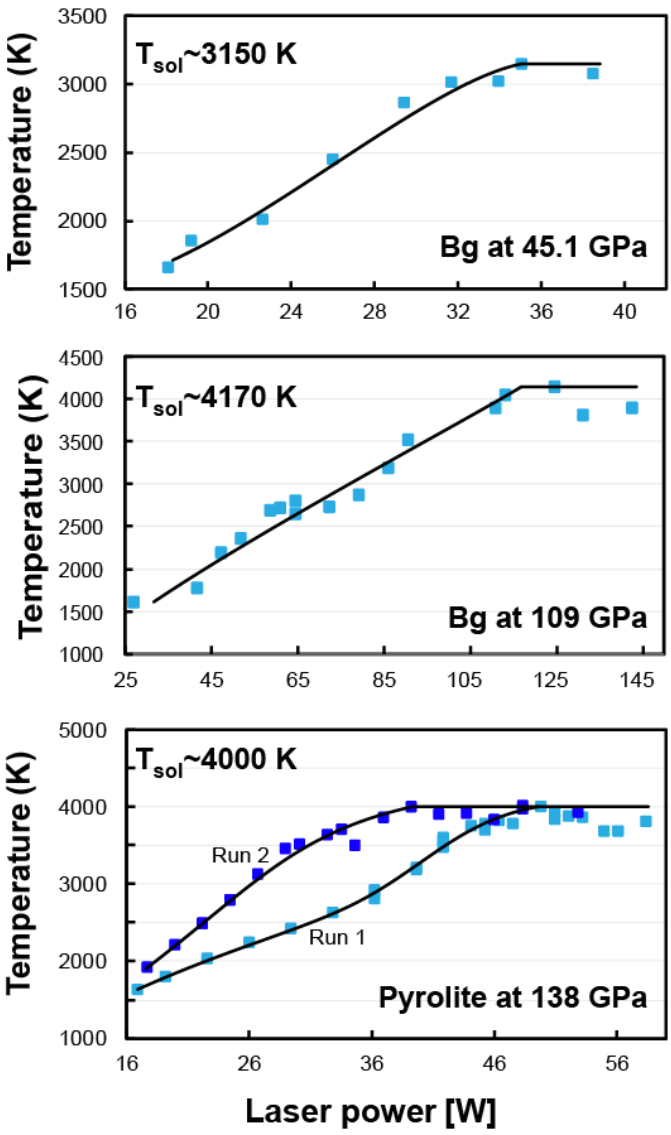
Suppl. Fig. 5: **Typical laser power vs temperature plateaus:** Evolution of the sample temperature with increasing laser power for bridgmanite at 45 GPa and 109 GPa (upper and middle frames) and pyrolite at 138 GPa (lower frame). Temperature remains below the solidus on the plateau; we therefore determine the solidus temperature by averaging the highest temperatures.